*minerals*

MDPI

*Article*

# The Rise of Proterozoic Diagenetic Spheroids Formed by Chemically Oscillating Reactions and Stimulated by Environmental Redox Changes

**Princess Aira Buma-at [1,2,3] and Dominic Papineau [3,4,5,6,*]**

[1] Department of Zoology, University of Cambridge, Cambridge CB2 3EJ, UK; pab219@cam.ac.uk
[2] University Museum of Zoology, University of Cambridge, Cambridge CB2 3EJ, UK
[3] Department of Earth Sciences, University College London, London WC1E 6BT, UK
[4] London Centre for Nanotechnology, University College London, London WC1H 0AH, UK
[5] Centre for Planetary Sciences, University College London and Birkbeck College London, London WC1E 6BT, UK
[6] Institute of Deep-Sea Science and Engineering, Chinese Academy of Sciences, Sanya 572000, China
* Correspondence: d.papineau@ucl.ac.uk

**Abstract:** Diagenetic spheroids are rounded mineralised structures in sedimentary rocks that span several orders of size dimensions. These objects include rosettes spanning tens of micrometres; millimetre-sized granules; and centimetre- to metre-scale botryoids, nodules, and concretions. Connections between diagenetic spheroids and chemically oscillating reactions (COR) have been established based on chemical and pattern similarities. Nevertheless, it is unknown if there are variations in their occurrences throughout geological time, especially during periods of global environmental change. This is because COR are pattern-forming reactions where carboxylic acids are decarboxylated by strong oxidants like sulphuric acid, bromate, or iodate. The hypothesis is that there should be a greater number of diagenetic spheroids at periods of increased atmospheric and oceanic oxygenation levels. Hence, this work presents the first compilation of occurrences of diagenetic spheroids between 0.541 and 1.8 billion years ago (Ga). The compiled patterned objects are those with concentric laminations and radially aligned crystals, which are patterns akin to equidistant circularly concentric waves that radially diffuse in COR. Another characteristic of diagenetic spheroids, similar to that found in botryoidal minerals, is the destructive interference that forms circular twins; this is identical to the COR pattern formed when circular waves meet. The timeline of Proterozoic diagenetic spheroids produced in this work reveals a significant increase in occurrences across the Ediacaran, which is attributed to an increased environmental oxidation state. During this interval, seawater is known to have become richer in sulphate and iodate, which create ideal conditions for the abiotic and diagenetic oxidation of biomass. Therefore, increased occurrences of diagenetic spheroids in the Neoproterozoic possibly represent sedimentological evidence for abiotic decarboxylation reactions and widespread COR in productive environments. The distribution of diagenetic spheroids observed during the Proterozoic may also be more broadly applicable to other epochs of Earth's history.

**Keywords:** concretion; botryoid; diagenesis; carbon cycle; fossilisation; Belousov–Zhabotinsky reaction

check for updates

**Citation:** Buma-at, P.A.; Papineau, D. The Rise of Proterozoic Diagenetic Spheroids Formed by Chemically Oscillating Reactions and Stimulated by Environmental Redox Changes. *Minerals* **2024**, *14*, 962. https://doi.org/10.3390/min14100962

Academic Editors: Hussein Kanbar and Mathieu Le Meur

Received: 6 August 2024
Revised: 14 September 2024
Accepted: 15 September 2024
Published: 24 September 2024

**Copyright:** © 2024 by the authors. Licensee MDPI, Basel, Switzerland. This article is an open access article distributed under the terms and conditions of the Creative Commons Attribution (CC BY) license (https://creativecommons.org/licenses/by/4.0/).

## 1. Introduction

Diagenesis includes all the biological, chemical, and physical processes that alter deposited sedimentary assemblages from sedimentation to erosion or metamorphism [1,2]. Concretions, nodules, botryoids, granules, and rosettes are mineralised spheroidal structures that are prevalent in the sedimentological record and usually relate to diagenesis. These objects can display circularly concentric and radial mineral patterns, a limited dominant mineralogy, and a common association with organic matter. They are also considered as abiotic in origin; hence, they are here grouped as 'diagenetic spheroids'. Diagenetic

spheroids are distinguished according to size ranges. Mega-concretions can have a diameter as large as several metres, and rosettes are the smallest type with diameters < $10^{-4}$ m [3]. Both concretions and nodules have sizes from $10^{-2}$ m to $10^{-1}$ m. Whereas the mineralogy of concretions is akin to its host rock, the composition of nodules differs from their surrounding sediments [4]. Granules are irregular spheroids that range between $10^{-2}$ m and $10^{-4}$ m in diameter. Botryoidal minerals include interconnected, or twinned, smooth spheroids, and their globular texture is grape-like, mammillary, or reniform in appearance [5]. Botryoids span a large diameter range from $10^{-1}$ m to $10^{-6}$ m.

Despite the array of descriptive terms, these objects commonly exhibit a sub-rounded morphology with circularly concentric and radially aligned geometric patterns [6–8]. Occasionally, they exhibit a triaxial ellipsoidal or lenticular morphology. The term diagenetic spheroids groups together those objects with identical ranges of patterns, which may imply a similar sedimentary and diagenetic history [5–10]. Typical mineral compositions of diagenetic spheroids include microcrystalline quartz (chert; chalcedony) [11,12], dolomite, pyrite, apatite, and/or organic matter [3,6]. Fossils may also be encapsulated in diagenetic spheroids and usually have a comparable mineral composition. For instance, well-preserved Ediacaran microfossils, like *Vendotaenia* sp. and *Oscillatoriopis obtusa*, have been identified within chert concretions in the Shibantan Lagerstätte [13–15].

The formation mechanism of diagenetic spheroids has yet to reach consensus. For instance, Dodd et al. (2018) disputed the wave action model for granules in granular iron formation on the basis that the arrangement of fine equidistant, circularly concentric laminations and radially aligned acicular crystals is improbable to form under turbulence. Moreover, shallow marine wave agitation cannot explain the common association of granules with organic matter and well-preserved microfossils. Diagenetic spheroids are considered abiotic precipitates and are therefore possible indicators of physicochemical processes [16,17]. However, nucleation-controlled growth around a central mass [18,19] is more likely to generate irregular clumps, rather than equidistant concentric laminations with density gradients. The Liesegang phenomenon is another abiotic process that is the purported origin of diagenetic spheroids [20], but it is unable to explain regular patterns of circular laminations [7]. Liesegang banding is produced by the precipitation and diffusion of metal cations within silica gels [20–22]. Moreover, Liesegang rings have a gravity-driven linear arrangement [23,24], in contrast with concentric rings observed in diagenetic spheroids.

Alternatively, Bosak et al. (2010) proposed that diagenetic spheroids associated with microbialites and stromatolites may be mineralised gas bubbles generated by photosynthetic microorganisms. Internal features, such as mineral inclusions and organic matter, are absent within bubbles [25]. The gas bubble theory therefore does not explain the occurrence of microfossils and concentric laminations in some diagenetic spheroids [3]. Occurrences of microfossils, degraded organic matter, or highly variable carbon and sulphur isotope compositions in diagenetic spheroids have been interpreted to suggest a biologically mediated formation [13,26–29]. For example, organic matter could act as nucleation sites, and mineral precipitation may be actively induced by microbial interaction with its niche [30].

COR have been proposed as an alternative formation model to explain the circularly concentric, radially aligned, and density gradient patterns often found in diagenetic spheroids [3,5–8,10–12,31]. Zaikin and Zhabotinsky (1970) report that "radial circular waves of oxidation were propagated" when phenanthroline ferrous sulphate (ferroin) was added to an aqueous solution of bromate, bromide, malonic acid, and sulphuric acid. Interference occurs when concentric waves from different initiation points intersect, producing 'interconnected round arcs' (or circular twins), known as Belousov–Zhabotinsky (B–Z) patterns [32]. B–Z reactions in Petri dishes display regular wave patterns and the effects of chemical turbulence. These circular waves span several size dimensions and are hence fractal patterns. In nature, abiotic carboxylic acids could be central to this reaction; alternatively, there are implications for biosignatures if the carboxylic acids are derived from biomass [3]. The radially propagating circles have been frequently recreated and analysed

in experimental settings [6,33–41]. Nevertheless, it was only recently proposed [5,7,8] that the patterns and products of COR are analogous with those of diagenetic spheroids. If COR occur naturally in the environment and indeed represent environmental proxies [12], then their occurrences might preserve evidence of global biogeochemical changes. In turn, if diagenetic spheroids form through COR, their occurrence in the rock record would represent direct sedimentological evidence for carbon cycling.

The Proterozoic spans from 2.5 to 0.541 Ga and includes a prolonged biogeochemical stasis between 1.8 and 0.8 Ga, dubbed the 'Boring Billion' [42,43], or, perhaps less anthropocentrically, the 'Balanced Billion' [44]. This interval is characterised by tectonic and environmental stability, with steady isotopic compositions of carbon, sulphates, and sulphides observed in marine sediments [45]. By contrast, the Neoproterozoic underwent large climatic variations due to major tectonic events like the Rodinian fragmentation and Gondwanan formation [46], as well as major glaciations. Cap carbonates, which are sedimentary sequences that record deglaciations, have calcite and dolomite with strong depletions in $^{13}C$. These have been variably interpreted as evidence for the oxidation of dissolved or suspended organic matter in the water column [47], local methane seeps [48], anaerobic oxidation of methane [49], or diagenetic oxidation of biomass in sediments [50]. Therefore, a timeline of the abundances of diagenetic spheroids in geological strata between 1.8 Ga (start of the 'Balanced Billion') and 0.541 (the Ediacaran–Cambrian boundary) may provide further insight into whether diagenetic spheroids are more likely to form under stable long-term geochemical conditions or dynamic ones, respectively. The emerging hypothesis is that an increased abundance of diagenetic spheroids near the end of the Neoproterozoic would be expected due to increased environmental oxidation because enhanced continental weathering provides an increased supply of dissolved ions in post glacial oceans. Based on a literature review, this work addresses two main scientific questions about diagenetic spheroids:

(a) Are there secular variations in the abundance of diagenetic spheroids during the Proterozoic?
(b) Could Proterozoic diagenetic spheroids represent sedimentological signatures of abiotic carbon cycling favoured by environmental oxidation?

## 2. Approach for a New Compilation

To determine the correlation between the occurrences of diagenetic spheroids during stable conditions and enhanced influxes of environmental oxygen, the abundance of concretions, nodules, botryoids, granules, and rosettes in sedimentological beds between 0.541 and 1.8 Ga was collected (Table 1). Secondary data were collected from widely available search engines like Google Scholar, Web of Science, and JSTOR, using key terms such as 'Proterozoic concretions', 'Proterozoic nodules', 'Proterozoic botryoids', 'Proterozoic granules', and Proterozoic rosettes'. Altogether, 72 occurrences of diagenetic spheroids from 33 formations were documented (Figure 1), and this dataset is up to date as of November 2024. Even though this is a comprehensive compilation of Proterozoic diagenetic spheroids, sample and formation bias is inherent within these collated data due to outcrop availability, the variable number of studies for each formation, the analytical approach used in publications, and whether authors reported occurrences of diagenetic spheroids of various sizes when they occurred. While these sampling biases are inherent to the geological and publication records, we argue that this compilation can still serve a useful purpose and show possible first-order trends. In the future, this compilation should be augmented and refined to hopefully create a momentum that stimulates the reporting of the occurrences of many more diagenetic spheroids, including those at microscopic scales.

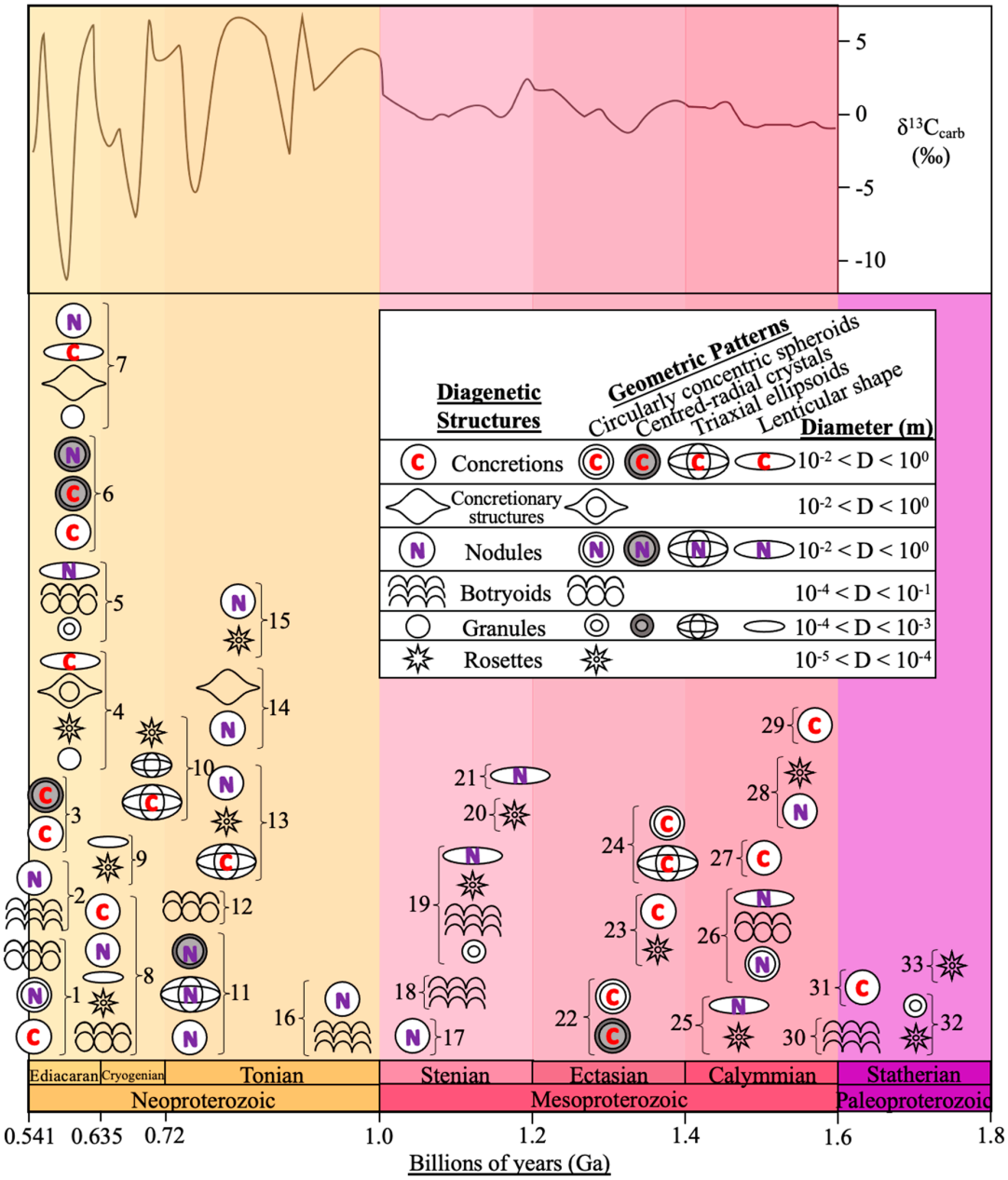


**Figure 1.** Distribution of various beds of diagenetic spheroids in Proterozoic strata and specifically between 1.8 and 0.541 Ga. The centre of the diagenetic structures' symbols is aligned to the median age of the formation, with age ranges and further mineralogical information simplified in Table 1. The dark grey outline indicates $\delta^{13}C_{carb}$ values across the Neoproterozoic and Mesoproterozoic interval obtained from Shields et al. (2019) and Li et al. (2022), respectively [51,52]. Numbers correspond to geological units: 1 = Dengying Formation; 2 = Omkyk Member, Northern Nama Group; 3 = Stáhpogieddi Formation; 4 = Ediacara Member; 5 = Tindir Creek; 6 = Ambed Formation; 7 = Bhander Limestone; 8 = Doushantuo Formation; 9 = Pioneer Sandstone; 10 = Wollogorang Formation; 11 = Backlundtoppen Formation; 12 = Beck Spring Dolomite; 13 = Bitter Springs Formation; 14 = Roan Group; 15 = Callanna Beds; 16 = Little Dal Group; 17 = Diabaig Formation; 18 = Nama Group; 19 = Apache Group; 20 = Bass limestone; 21 = Milbeena Bore; 22 = Independence Fjord Group; 23 = Newland Formation; 24 = Xiamaling Formation; 25 = Helena Formation; 26 = Amelia Dolomite and Mallapunyah Formation; 27 = Jixian System; 28 = Mount Isa Mine; 29 = Gaoyuzhuang Formation; 30 = Espinhaço Supergroup; 31 = Barney Creek Formation; 32 = Frere Formation; 33 = Athabasca Group; see Table 1 for more information.

**Table 1.** Proterozoic Diagenetic Spheroids.

| | Geological and Geographical Location | Age Range (Ga) | Type of Diagenetic Spheroid | Mineralogy of Structures | Host Rock Facies and Associated Sediments | References |
|---|---|---|---|---|---|---|
| 1 | Dengying Formation, Yangtze Craton, South China | 0.545 to 0.551 | Botryoids, nodules, concretions | Dolomite, chert unspecified carbonate mineral | Dolomite laminated micritic and bituminous limestone with abundant fossils | [7,15,53,54] |
| 2 | Omkyk Member, Northern Nama Group, Namibia, Africa | ca. 0.5488 | Nodules, botryoids | Calcite with dolomitized stromatolite crust | Fossiliferous carbonate, siliclastic rocks | [55] |
| 3 | Stáhpogieddi Formation, Digermulen Peninsula, Arctic Norway | ca. 0.563 | Concretions | Calcite | Siliclastic sedimentary rocks | [56] |
| 4 | Ediacara Member, Rawnsley Quartzite, Flinders Ranges, South Australia | 0.541 to 0.635 | Concretions, concretionary structures, rosettes, granules | Silica, quartz, and clay coating | Feldspathic sandstone | [57] |
| 5 | Tindir Creek, Yukon Territory, Canada | 0.541 to 0.635 | Nodules, botryoids, granules | Chert with organic coating | Limestone, shale | [58] |
| 6 | Ambed Formation, Bou Azzer mining district, Anti-Atlas, Morocco | 0.58 to 0.615 | Nodules, concretions | Unspecified silicate mineral with cobalt loellingite accessory crystals and red clays (smectites, talc, chlorite) | Interlaminated siliceous and carbonaceous facies | [59] |
| 7 | Bhander Limestone, Thoman River, Maihar, central India | 0.544 to 0.65 | Nodules, concretions, concretionary structures, granules | Calcic spar, K-feldspar nuclei, glauconite, unspecified carbonate mineral | Limestone | [60,61] |
| 8 | Doushantuo Formation, central South China | 0.551 to 0.632 | Concretions, nodules, granules, rosettes, botryoids | Chert, apatite pyrite organic matter | Algal and siliceous dolomite, black shale, limestone and phosphorite | [62,63] |
| 9 | Pioneer Sandstone, Northeastern Amadeus Basin, Australia | 0.58 to 0.709 | Granules, rosettes | Quartz, feldspars, barite | Feldspathic sandstone phosphorite | [64,65] |
| 10 | Wollogorang Formation, McArthur Basin, northern Australia | ca. 0.705 | Concretions, rosettes, granules | Dolomite, quartz, pyrite | Black shales, mudstone, siltstone, sandstone conglomerates | [66] |
| 11 | Backlundtoppen Formation, Spitsbergen, Svalbard | 0.7 to 0.8 | Nodules | Chert, chalcedony | Oolitic, pisolitic, cherty limestone, dolomite | [67,68] |
| 12 | Beck Spring Dolomite, eastern California | 0.73 to 0.78 | Botryoids | Acicular dolomite, aragonite or calcite, strontium rich | Dolomite limestone | [69,70] |

**Table 1.** *Cont.*

| | Geological and Geographical Location | Age Range (Ga) | Type of Diagenetic Spheroid | Mineralogy of Structures | Host Rock Facies and Associated Sediments | References |
|---|---|---|---|---|---|---|
| 13 | Bitter Springs Formation, Australia | ca. 0.8 | Concretions, nodules, rosettes | Chert, carbonate, silica anhydrite, bipyramidal quartz | Biostromal stromatolites, mudstone, dolomite and red beds | [71,72] |
| 14 | Roan Group, Katangan Basin, Zambia, Africa | 0.735 to 0.883 | Concretionary structures, nodules | Anhydrite, dolomite | Arkose with siltstone and clastic carbonate interbeds | [73] |
| 15 | Callanna Beds, Willouran Ranges, South Australia | 0.802 to 0.827 | Nodules, rosettes | Chert, sulphate (barite, anhydrite, or gypsum) | Cherty pyritic, carbonaceous dolomite with siltstone | [74,75] |
| 16 | Little Dal Group, Mackenzie Mountains, Canada | 0.8 to 1.1 | Nodules, botryoids | Calcite, quartz | Limestone, carbonate shale | [76,77] |
| 17 | Diabaig Formation, Torridonian Succession, northwest Scotland | 0.994 to 1.09 | Nodules | Apatite, organic matter | Rhythmically alternating mudstone and sandstones, micro-fossiliferous | [78] |
| 18 | Nama Group, Damara Supergroup, Namibia, Africa | 1 to 1.2 | Botryoids | Carbonate, calcite, iron-rich clays and hematite | Siliclastic sedimentary rocks | [79,80] |
| 19 | Mescal Limestone and Troy Quartzite, Apache group, Arizona, North America | 1.1 to 1.4 | Nodules, rosettes, botryoids, granules | Chert, dolomite, gypsum, chalcedony, quartz | Alternating, thinly laminated dolomite and chert-rich dolomite, sandstones | [81] |
| 20 | Bass limestone, Bright Angel Canyon, Arizona, USA | 1.1 to 1.255 | Rosettes | Chert | Limestone | [82,83] |
| 21 | Milbeena Bore, Manganese Group, Western Australia | 1.05 to 1.317 | Nodules | Braunite, clay, apatite, unspecified carbonate mineral | Well bedded micaceous to sandy shale and siltstone | [84–86] |
| 22 | Independence Fjord Group, North Greenland | 1.23 to 1.38 | Concretions | Silica-cemented, carbonate, dolomite, quartz | Sandstone siltstone | [87] |
| 23 | Newland Formation, Belt Supergroup, USA | 1.325 to 1.4 | Concretions, rosettes | Pyrite, barite, gypsum | Shale | [88] |
| 24 | Xiamaling Formation, North China | 1.35 to 1.4 | Concretions | Calcite, clay (illite, chamosite), ankerite, or siderite | Green silty shale (mainly glauconite and silty quartz) | [89–91] |
| 25 | Helena Formation, Central Cordillera, North America | 1.44 to 1.5 | Nodules, rosettes | Dolomite, quartz | Mudstone, sandy grainstone, stromatolites | [92] |
| 26 | Amelia Dolomite and Mallapunyah Formation, McArthur Basin, Northern Territory, Australia | 1.4 to 1.6 | Botryoids, nodules | Chalcedony anhydrite chert | Dolomite, sandstones, quartz arenite | [93] |

**Table 1.** *Cont.*

| | Geological and Geographical Location | Age Range (Ga) | Type of Diagenetic Spheroid | Mineralogy of Structures | Host Rock Facies and Associated Sediments | References |
|---|---|---|---|---|---|---|
| 27 | Jixian System, Yanliao basin, North China Craton | 1.4 to 1.6 | Concretions | Chert | Stomatolitic and bituminous very finely crystalline dolomite | [94] |
| 28 | Mount Isa mine, Queensland, Australia | 1.5 to 1.6 | Rosettes, nodules | Chert | Dolomite | [95] |
| 29 | Gaoyuzhuang Formation, Yanshan area, North China | 1.54 to 1.6 | Concretions | Unspecified carbonate mineral | Calcareous mudstone dolomite | [96] |
| 30 | Espinhaço Supergroup, Minas Gerais, Brazil | 1.5 to 1.73 | Botryoids | Thin titanium oxide coating, hematite, hongshiite | Quartzite, conglomerate | [97] |
| 31 | Barney Creek Formation, McArthur Basin, Northern Territory, Australia | ca. 1.639 | Concretions | Unspecified carbonate mineral organic matter | Shale | [98] |
| 32 | Frere Formation, Nabberu Basin, Western Australia | ca. 1.7 | Granules, rosettes | Chert, hematite, greenalite, organic matter, stilpnomelane | Stromatolites, granular iron formation | [10,99] |
| 33 | Athabasca Group, Athabasca Basin, Canada | 1.7 to 1.75 | Rosettes | Trioctahedral chlorite (clinochlore) | Quartz-rich sandstone, conglomerate | [100] |

## 3. Observations from the Compilation of Proterozoic Spheroids

### *3.1. Geometric Patterns of Diagenetic Spheroids*

Concentric lamination patterns are displayed when multiple circles share the same centre. Within Proterozoic diagenetic spheroids, these are the most common type of geometric pattern, with 43% of the total collated diagenetic spheroids displaying circular laminations. However, this value is likely underestimated because the internal geometry of 36 compiled spheroids remains undetermined. Figure 2b shows an example of a calcite concretion with circularly concentric layers and coloured mineral gradients. Botryoidal dolomite from the Dengying Formation (Figure 2c,d) demonstrates the formation of circular twins at the junctions where concentric laminations meet and destructively interfere. This arrangement can be considered as an example of crystal twinning within botryoidal minerals, which vary in size across several orders of magnitude. Irregularly shaped cavity structures also form upon the destructive interference of circularly concentric laminations (Figure 2a). Variations in geometric patterns are dependent on the extent of the convergence of individual concentric circles. Therefore, fractal geometry occurs, since self-similar and circularly concentric patterns are observed at regular intervals over several orders of size magnitudes in Proterozoic diagenetic spheroids.

Centred radial patterns are also commonly exhibited geometric patterns in diagenetic spheroids, with five instances recorded during the Proterozoic (Figure 1). These are self-similar with circularly concentric patterns, but with the addition of radial fibrous crystals that have darker coloured banded zones emanating from a singular centre point. The laminations observed in Figure 2d have rhythmically oscillating thin dark and thick brighter laminae with sharp boundaries. The dark and bright laminae are syntaxial, with the lighter laminae containing larger dolomite crystals [54]. Lenticular and triaxial ellipsoids are infrequent patterns and are typically demonstrated by nodules and concretions. Ellipsoidal

shapes in diagenetic spheroids may be due to the original morphology of decomposing clumps of biomass [101].

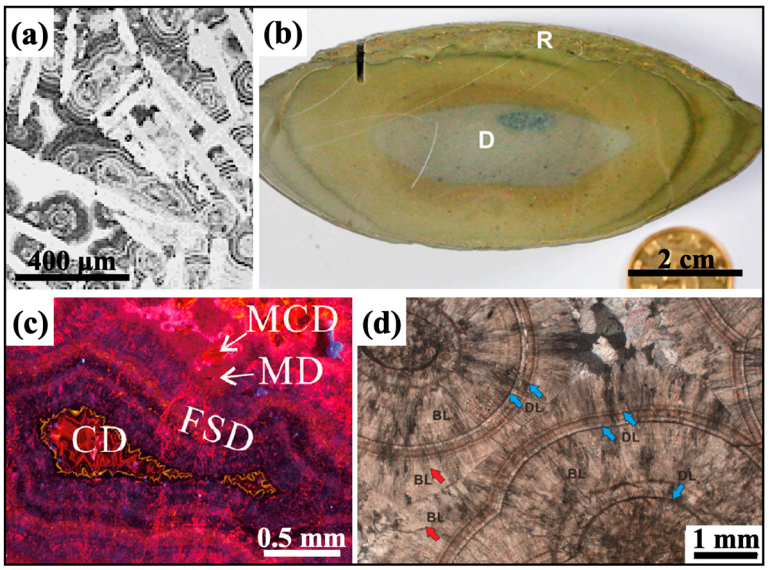


**Figure 2.** A selection of common geometric patterns observed within diagenetic spheroids. (**a**) Botryoidal gypsum forms filled with quartz and acicular pseudomorphs from the 1.1 to 1.4 Ga basal Troy Quartzite in Arizona [81]. (**b**) Calcite concretion with concentric ring structures from the Xiamaling Formation, 1.35 to 1.4 Ga [90]. The "D" marks displacive growth, whilst "R" displays the areas of replacive growth [90]. (**c**) Cathodoluminescence photomicrograph displaying a cavity structure of botryoidal dolomite from the Dengying Formation [53]. Crystalline dolomite (CD) cements and fascicular slow dolomite (FSD) cements are indicated, as well as micritic dolomite (MD) and microcrystalline dolomite (MCD). (**d**) Botryoidal laminations from the Dengying Formation (0.545 to 0.551 Ga) in the Gaojiashan outcrop [54]. Blue arrows showcase dark lamina (DL), whereas red arrows point towards brighter lamina (BL) [54]. All figures reproduced with permission.

### *3.2. Mineralogy and Palaeontology of Diagenetic Spheroids*

Chert (microcrystalline quartz) is the most common mineral observed in diagenetic spheroids, with 12 out of 72 occurrences of diagenetic spheroids exhibiting a chert mineralogy. Nine carbonate spheroids and one silicate spheroid are recorded, but both lack specificity since these terms represent unspecified mineral groups. For example, the typical anhydrous carbonate minerals are calcite, aragonite, and dolomite. Quartz and feldspars are common types of diagenetic silicates, but further petrographic analyses of thin sections should be conducted more commonly on diagenetic spheroids to further determine their mineralogy. Quartz occurrences (8), dolomite occurrences (7), and calcite (6) are the next most common major minerals (see Table 1). Moreover, phosphorite nodules in siliceous dolomite and micritic limestone are abundant in the Doushantuo Formation in China [62]. Botryoidal apatite occurs among granules in black organic-rich phosphorite of the Doushantuo Formation [63]. Pyritic concretions also occur in the Mesoproterozoic Newland Formation in North America [88].

Seven recorded Proterozoic diagenetic spheroids occur in shallow marine deposits associated with stromatolites or microbialites. In the Namibian Omkyk Member near the end of the Ediacaran, nodules are encrusted by a rim of dolomitised microbial laminates and contain various microfossils (Figure 3a–c) [55]. These purported metazoans are biomineralised and are oriented perpendicular to a fissure wall [55]. Ediacaran microfossils can also be observed within diagenetic spheroids from China's Shibantan Lagerstätte [15]. Chert nodules from the Shibantan Member of the Dengying Formation also contain well-preserved microfossils such as *Oscillatoriopsis obtusa* (Figure 3d) [14]. Although the phylogenetic affinities of these microfossils are undetermined, due to their morphological similarity

to photoautotrophs, they have been interpreted as benthic cyanobacteria [15]. These observations and inferences have also been made in the Doushantuo Formation where apatite granules commonly contain a range of microfossils [63]. There are also well-preserved microfossils inside concretions of bitumen and chert from the Mesoproterozoic Xiamaling Formation in northern China [89]. In chert granules from the Late Paleoproterozoic Frere Formation, subspherical and filamentous microfossils are clustered together and exhibit varying degrees of mineralisation, whereas most are encrusted with a relatively thick layer of iron oxides [99].

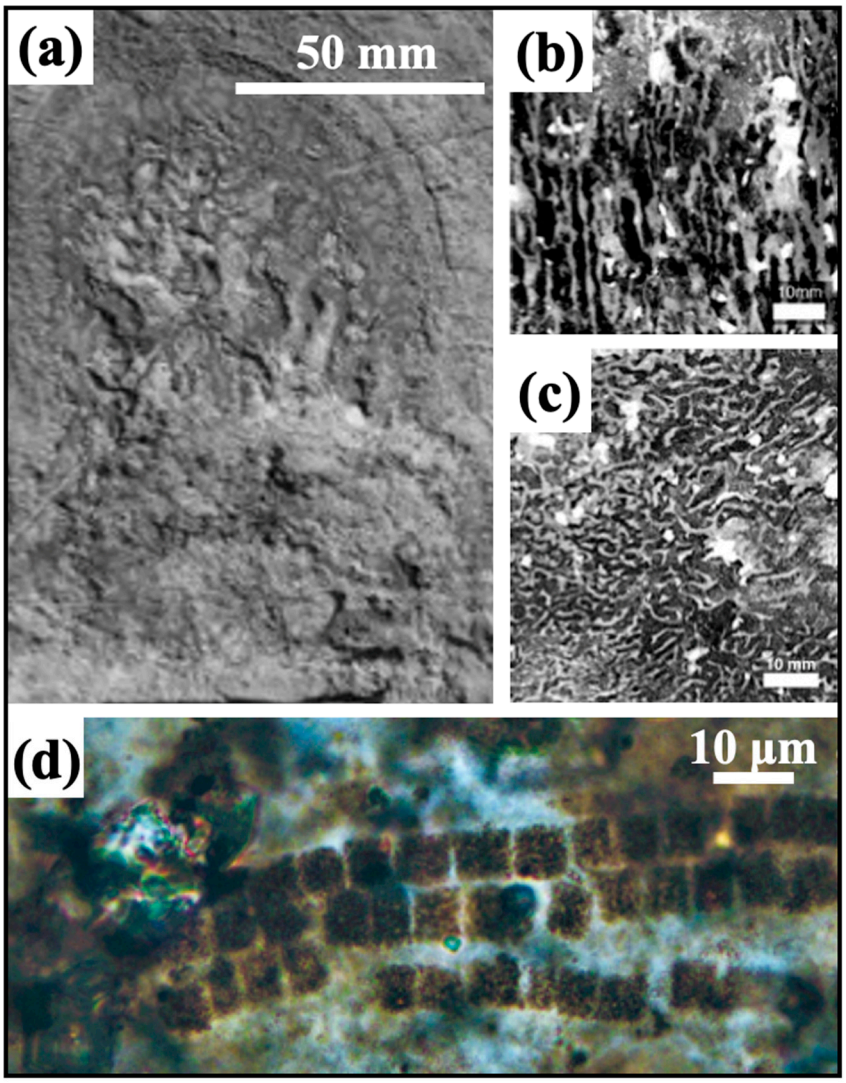


**Figure 3.** Microfossil occurrences in Proterozoic diagenetic spheroids. (**a**) Outcrop image of nodules containing *Namapoikia rietoogensis* from the Omkyk Member, Nama Group, southern Namibia [55]; (**b**) Longitudinal holotype [55]; and (**c**) Transverse section [55]. (**d**) *Oscillatoriopsis obtusa* from the Shibantan Lagerstätte [15]. Figures reproduced with permission.

### *3.3. Distribution Trend of Diagenetic Spheroids*

A greater number of occurrences of diagenetic spheroids during the Neoproterozoic, especially in the Ediacaran, can be observed compared to the Mesoproterozoic (Figure 1). The highest frequency of diagenetic spheroids thus coincides with positive excursions of $\delta^{13}C_{carb}$ values [51,102], which is a major proxy for increased atmospheric oxygen. By contrast, a limited number of spheroids occur in the 0.8–1.8 Ga interval, which coincides with the 'Balanced Billion'. For instance, a significant decrease in diagenetic spheroids occurs during the early Tonian because only two diagenetic spheroid occurrences from the

Mackenzie Mountains in northwestern Canada have been recorded. There also appears to be no considerable changes in the number of diagenetic spheroids within the Mesoproterozoic, with a roughly similar amount across the Stenian, Ectasian, and Calymmian (Figure 1).

## 4. Discussion

### *4.1. Geometric Patterns in Proterozoic Diagenetic Spheroids Compared to Those of COR*

Under standard conditions, an unperturbed B–Z reaction produces random oxidation spots that propagate as a series of equidistant concentric rings [32]. Once a significant number of chemical waves have accumulated, destructive interference between waves occur (Figure 4b,c). At late reaction stages, linearly elongated cavities and twinned patterns occur at sites where chemical waves are mutually annihilated, causing the erasure of wave traces [6,7].

The geometric patterns produced by COR are self-similar to the circularly concentric patterns found in diagenetic spheroids. Figure 4a shows an example of equidistant concentric laminations with no interference, perfectly recreating some of the COR patterns. Moreover, sub-parallel wavy layers caused by circular twins can be recreated by B–Z reactions due to destructive interference (Figure 4b). This effect appears related to surface tension in botryoids where the layers usually follow the cavity inside lining, whereas in a Petri dish, the sub-parallel layers follow the glass wall. Circularly concentric waves can also have imperfect equidistant or non-equidistant laminations [5,39], which is akin to the variable spacing distance displayed by laminations in some diagenetic spheroids. Mineral colour density gradients are also apparent in Figure 4b. Asymmetric irregular ellipses of concentric chemical waves are due to a higher concentration of nucleation spots and the resulting twins between chemical waves during radial diffusion (Figure 4c). Other diagenetic spheroids with these kinds of self-similar patterns that have previously been attributed an origin influenced by COR include rosettes of quartz ± apatite ± haematite ± carbonate ± organic matter [10,31]; botryoids of malachite, quartz, and dolomite + organic matter [3,5,7,11,12]; granules of quartz ± apatite ± haematite ± magnetite ± organic matter ± dolomite ± pyrite [6,10]; and concretions or nodules of quartz ± haematite ± carbonate ± organic matter ± pyrite [7,8].

Oxidation spots in COR are chaotically distributed [103], which is akin to the random locations of diagenetic spheroids within sedimentary layers. Hastings et al. (2003) argued against random initiation by attributing microscopic fluctuations in the concentration of reactants to the initial nucleation of chemical activity [104]. Despite the unpredictability of COR, these reactions produce self-similar patterns such as circularly concentric equidistant laminations, twinned circles, cavity structures, radial diffusion, and colour gradients in laminations. All these self-similar patterns closely resemble those found in Proterozoic diagenetic spheroids (Figure 4). Oxidation spots with circularly concentric laminations in COR experiments have diameters that span sub-millimetre to decimetre sizes [32,41]. Therefore, COR display fractal patterns, akin to the fractal nature of patterns displayed by diagenetic spheroids.

Furthermore, radially aligned crystals in diagenetic spheroids are often displayed (Figures 2d and 4b), and they are similar to the radial diffusion observed in COR. There are also strong colour gradients produced during COR, which are analogous to alternating light and dark mineral laminations of iron oxide and organic matter within circularly concentric spheroids (Figures 2d and 4b,c). The characteristic red and blue seen in COR experiments is produced via ferroin reduction and oxidation, respectively [41]. The oscillatory patterns displayed in Figure 4 are initiated inside a ten-centimetre diameter glass Petri dish and require a film of COR solution [7]. Less distinguished chemical waves and cavity structures become apparent when some of the reactants are exhausted after around 30 min [35]. During diagenesis, COR must occur three-dimensionally and at much larger scales, which is a limitation not yet demonstrated by COR experiments. Furthermore, COR experiments in Petri dishes can be restarted when the solution is shaken, which suggests that COR in

nature would occur during the early stages of burial diagenesis, under calm conditions and within relatively short time scales. Nevertheless, it likely took longer in environmental settings than in COR experiments due to the expected lower concentration of reactants. Despite these limitations, patterns of circularly concentric laminations, colour gradients, radial geometry, twins, and cavities are found both in COR and in diagenetic spheroids (Figure 4), which constitutes a solid basis to argue for COR as a model for the formation of diagenetic spheroids.

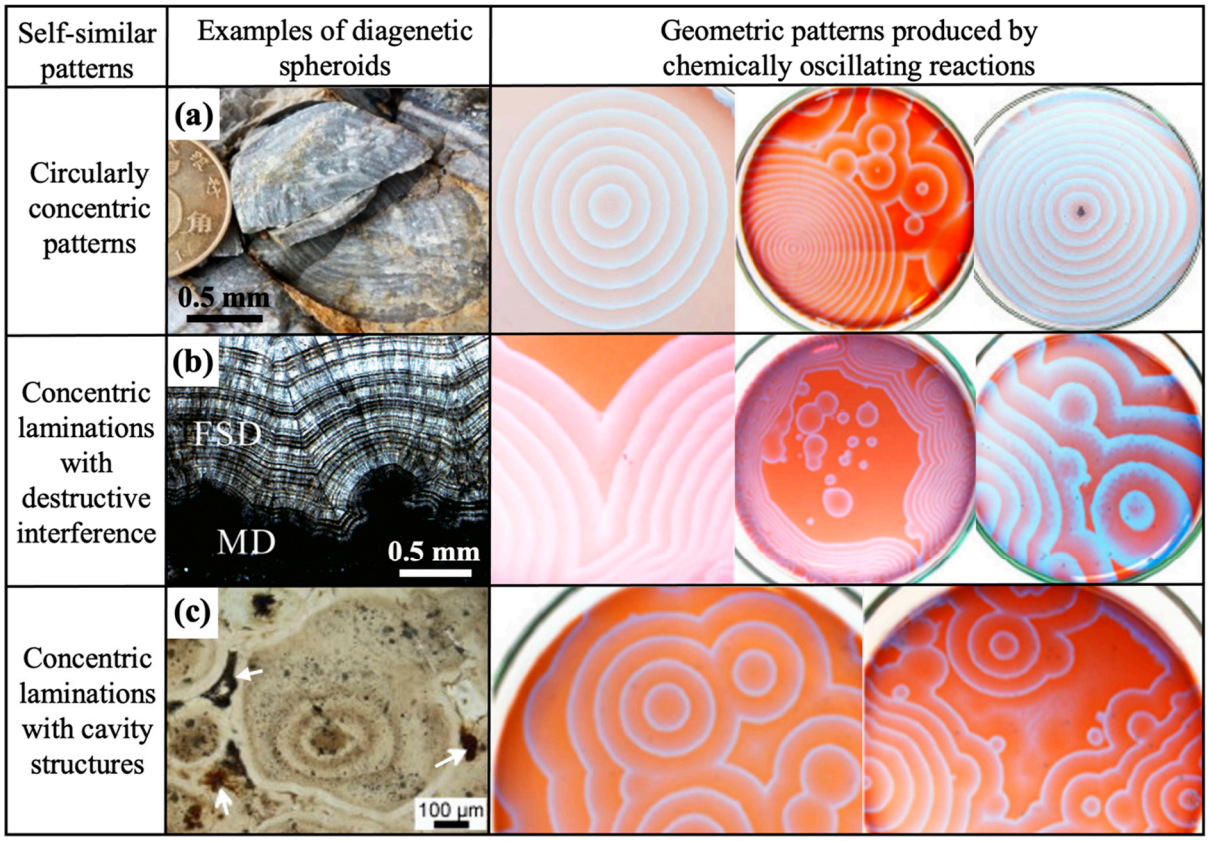


**Figure 4.** Summative grid to compare the self-similar geometric patterns of diagenetic spheroids, shown in plane-polarised light, with those produced by COR. The COR experimental images are from Papineau et al. (2021), and Petri dishes are 10 cm in diameter [7]. (**a**) Carbonate–apatite concretion with a circularly concentric lamination pattern in phosphorite, Doushantuo Formation in China (Papineau et al., in review). (**b**) Botryoids composed of fascicular slow dolomite (FSD) cements with chemical growth zonations, radial geometry, and circular twins that grew from a microbialite substrate found in the Dengying Formation, Yangtze Craton [53]. The abbreviation MD stands for micritic dolomite [53]. (**c**) Apatite granule from the Doushantuo Formation that shows concentric gradients of brown-coloured organic matter along with white arrows indicating linearly elongated cavity structures [63]. Figures reproduced with permission.

### *4.2. Comparison of Substances in COR and Proterozoic Diagenetic Spheroids*

Experimental COR begin when a redox-sensitive metal-based catalyst is added to a solution with a strongly oxidising halogen, its complementary halide salt, malonic acid, and sulphuric acid [32,39]. Variable concentrations can be utilised to initiate COR, and there are various reactants that can produce B–Z patterns [36,39]. Although many chemical reactions can occur during COR formation, two equations are particularly important:

$$2Fe^{2+} + BrO_3^- + HBrO_2 + 3H^+ \leftrightarrow 2Fe^{3+} + 2HBrO_2 + H_2O + 2e^- \quad (1)$$

$$3CH_2(COOH)_2 + 4BrO_3^- \rightarrow 4Br^- + 9CO_2 + 6H_2O \quad (2)$$

In Equation (1), iron in phenanthroline ferrous sulphate (ferroin) is oxidised from $Fe^{2+}$ to $Fe^{3+}$, which causes the observed colour change. In Equation (2), the reaction involves decarboxylation of malonic acid (or other carboxylic acids), the production of carbon dioxide (seen as bubbles in COR experiments), and a change in the oxidation state of bromine from +5 to −1. In COR, the chemical composition of products and intermediates remains undetermined, yet it can be predicted that the chemical waves are composed of variably oxidised ferroin and halogenated carboxylic acids [7].

The concentration of bromide ions ($Br^-$) has been argued to control the oscillating nature of the B–Z reaction (Orbán et al., 2001) [40]. When $Br^-$ exceeds the critical level, the oxidation of iron in ferroin is favoured, which generates a colour change in the diffusing circular waves from red ($Fe^{2+}$) to blue ($Fe^{3+}$). Other metals can also act as possible catalysts in COR [39]. The reaction is thought to terminate when electron donor molecules like carboxylic acids or electron acceptors like bromate are exhausted or become too low in concentration [5]. Therefore, diagenetic environments that can concentrate reactants are ideal, such as evaporitic environments where halogens, sulphate, and biomass can accumulate.

Carboxylic acids and ketones are examples of other organic acids that can initiate COR [6,39,40]. In nature, carboxylic acids are abundant because they are natural constituents of biomass, which decays in part through decarboxylation reactions [105–107]. Spheroidal microfossils such as *Oscillatoriopsis obtusa* and *Namapoikia rietoogensis* occur in Proterozoic diagenetic spheroids (Figure 3a–d [15,55]), and other Proterozoic microfossils commonly occur in diagenetic spheroids [63,89]. Subspherical and filamentous microfossils occur in granules from the late Palaeoproterozoic Frere Formation in the Nabberu Basin, and they often exhibit iron oxide encrustation [99]. The association of organic matter with iron oxides and pyrite could be because these minerals can be products of microbial sulphate reduction [108,109]. However, disseminations of iron oxides, pyrite, carbonate, and organic matter in diagenetic spheroids composed of quartz can also be interpreted to arise from abiotic COR because these can constitute the self-similar patterns [7,8,12]. In addition, some diagenetic spheroids also contain both sulphides like pyrite and sulphates like gypsum, anhydrite, or barite. All these mineral substances are like those in COR because they involve iron, carbon, and sulphur compounds with variable oxidation states, which is an important phenomenon in COR. The common occurrence of authigenic quartz in diagenetic spheroids can be interpreted to represent alkalinity generated during early diagenetic decomposition of biomass. Silica and high pH are different from the usually acidic conditions of COR, but they do not impede on pattern formation in COR [7]. Other approaches are needed to distinguish contributions from biological sulphate reduction and abiotic sulphate reduction in diagenetic spheroids, such as through large ranges of sulphur isotope ratios. However, COR have not yet been investigated for stable isotope fractionation on sulphur, carbon, iron, or halogens. Therefore, the abiotic putrefaction of microbial biomass in diagenetic environments is a likely process that uses organic acid reactants for COR [7]. The COR model can thus elegantly explain why Proterozoic diagenetic spheroids are often associated with fossils and organic matter.

For COR to occur naturally, productive, oxidising, and evaporitic diagenetic environments are well-suited to decompose microbial biomass. Table 1 displays the variety of environments considered in this study and shows that limestone, phosphorite, chert, and quartzitic sandstone most commonly contain diagenetic spheroids. The preservation of perfectly equidistant circularly concentric laminations, radially aligned crystals, and a limited range of chemical composition is not immediately compatible with the wave action model for the formation of diagenetic spheroids like botryoids and granules [110–113]. Hence, while wave action cannot be excluded to play a role in rounding granules for instance [10], it should be considered an insufficient model to explain the occurrence of specific geometric patterns within. The gas bubble model [25] can also be ruled out based on its inability to explain why microfossils are commonly inside diagenetic spheroids. Considering their circular concentricity, mineralogy, and inclusions of organic matter and

common microfossils, the COR model is the most convincing model for the formation of diagenetic spheroids [3,5–8,10–12,31].

During early diagenesis, the oxidation of organic acids through the decarboxylation of organic matter was likely needed to initiate COR and produce spheroidal objects [6,7]. Originally, colloidal silica is present under alkaline conditions. However, when carboxylic acids undergo decarboxylation, acid is produced, and the pH is lowered [7]. If this occurs under alkaline conditions, it results in the precipitation of minerals, such as quartz, apatite, carbonate, and pyrite [8]. Microcrystalline quartz, cryptocrystalline apatite, micritic carbonate, nanoscopic pyrite and hematite, and finely disseminated organic matter are all commonly found within diagenetic spheroids (Table 1). Hence, these minerals are consistent with the COR model of diffusing reaction products and intermediates in colloidal gels with its consequent permineralisation under pH gradients. Therefore, in addition to the variety of geometric patterns, the mineralogy and chemical substances of diagenetic spheroids can also be explained by the COR model.

### *4.3. Influences of Atmospheric Oxygenation on Occurrences of Diagenetic Spheroids*

Most diagenetic spheroids occur during the Neoproterozoic era (Figure 1). The increase in occurrences coincides with intense variations in $\delta^{13}C_{carb}$, ranging from −10 to +10‰ [51], which is a well-known proxy for atmospheric oxygenation. Therefore, this is an indication that major perturbations in the carbon cycle are linked to increased occurrences of diagenetic spheroids and thus of COR naturally occurring in environmental settings. This observation also supports the COR model for the formation of circularly concentric laminations in diagenetic spheroids and for the preservation of microfossils in diagenetic spheroids. This is further supported by the smaller number of diagenetic spheroid occurrences during the 'Balanced Billion', when perturbations in $\delta^{13}C_{carb}$ were significantly smaller, stagnating mostly near 0‰ [51].

Under increased environmental oxygen, higher chemical weathering rates, and intense greenhouse conditions, more cations and anions are delivered into sea water [114]. Hence during the Ediacaran, iodate, bromate, and sulphate levels in seawater increased [114], thereby providing an increased availability of COR reactants. Post-glacial Neoproterozoic rocks of marine sedimentary origin also show increased variations in $\delta^{34}S_{sulphate}$ and $\delta^{34}S_{sulphide}$, which imply increased availability of seawater sulphate [115,116]. Oxidised sulphur species can act as electron acceptors in the remineralisation of organic carbon by sulphate-reducing bacteria, or abiotically as in the case of COR in the environment. Primary productivity of organic matter also increased during the Neoproterozoic and promoted a profound expansion of ecosystems because sulphate and phosphate play central roles in biochemistry [117]. This biosphere expansion would enable an increased availability of biomass and carboxylic acids, which again are key reactants in COR. Lastly, environmental oxygenation during the Neoproterozoic would also have contributed to create redox gradients and thermodynamic disequilibria in sedimentary marine environments, thereby further stimulating COR.

A natural progression of this study includes the expansion of the considered age range to encompass the Phanerozoic eon (0.541 Ga until modern times) as well as the Paleoproterozoic era and Archean eon. This study provides valuable new insights on the influence of intense variations in $\delta^{13}C_{carb}$ on the prevalence of diagenetic spheroids in sedimentary rocks, and it is likely also applicable to the Paleoproterozoic. An almost symmetrical distribution of the occurrences of diagenetic spheroids, with greater amounts at both ends of the Proterozoic, would therefore further support the newly proposed COR model. Since the connection between COR and diagenetic spheroids is still in its infancy, broader documentation of these spheroidal structures is needed to search for additional occurrences. This may eventually confirm that the COR model applies to most types of diagenetic spheroids throughout Earth's history. Diagenetic spheroids should thus be regarded as sedimentological patterns produced abiotically from carbon cycling with carboxylic acid reactants and $CO_2$ products. While carboxylic acids are most likely

of biological origin in most environments (on Earth), they may also be abiotic in origin, for instance in hydrothermal vent systems where Fischer–Tropsch type synthesis takes place [118]. Hence, this study may even apply more broadly to oceanography, planetary sciences, and exobiology.

## 5. Conclusions

The classical COR is the B–Z reaction, which produces characteristic fractal patterns and $CO_2$ bubbles from reactants such as malonic acid, bromate-bromide, sulphuric acid, and ferroin. Self-similar fractal patterns, such as circularly concentric laminations, radial geometries, twins, and linearly elongated cavities occur in diagenetic spheroids and are identical to those produced by COR. These diagenetic spheroids include concretions, nodules, botryoids, granules, and rosettes. Similarities between chemical reactants and products of COR and diagenetic spheroids have also been elucidated based on chemical substances. Hence, diagenetic spheroids are interpreted to be formed by COR based on their patterns and substances, and they can thus be considered as evidence of abiotic carbon cycling.

Because biomass is enriched in carboxylic acids, organic matter in sediments is affected by decarboxylation during the formation of diagenetic spheroids; hence, the COR model explains why fossils and microfossils are common in these mineralised objects. In this first compilation of occurrences of diagenetic spheroids over geological history between 0.541 and 1.8 Ga, a secular peak in the frequency of their occurrences is documented during the late Neoproterozoic. This observation is consistent with the COR model because the Neoproterozoic oxygenation event resulted in high levels of biomass, increased oxidative weathering, and greater amounts of oxidants, such as iodate and sulphate, all of which are linked to reactants in COR. These conditions during the Neoproterozoic were favourable to COR and resulted in increased occurrences of diagenetic spheroids in sedimentary rocks from this era. This study is a prelude to others that will cover the rest of Earth's history.

**Author Contributions:** Conceptualization, D.P.; methodology, D.P. and P.A.B.-a.; formal analysis, D.P. and P.A.B.-a.; investigation, P.A.B.-a.; writing—original draft preparation, P.A.B.-a.; writing—review and editing, D.P. and P.A.B.-a.; visualization, P.A.B.-a.; supervision, D.P.; project administration, D.P. All authors have read and agreed to the published version of the manuscript.

**Funding:** This research received no external funding.

**Data Availability Statement:** No new data were created in this study. All data can be found in the cited references.

**Conflicts of Interest:** The authors declare no conflict of interest.

## References

1. Curtis, C.D. Geochemistry: Sedimentary geochemistry: Environments and processes dominated by involvement of an aqueous phase. *Philos. Trans. R. Soc. A* **1977**, *286*, 353–372.
2. Burley, S.D.; Kantorowicz, J.D.; Waugh, B. Clastic diagenesis. *Geol. Soc. Spec. Publ.* **1985**, *18*, 189–226. [CrossRef]
3. Gabriel, N.W.; Papineau, D.; She, Z.; Leider, A.; Fogel, M.L. Organic diagenesis in stromatolitic dolomite and chert from the late Palaeoproterozoic McLeary Formation. *Precambrian Res.* **2021**, *354*, 106052. [CrossRef]
4. Mitsuchi, M. Characteristics and genesis of nodules and concretions occurring in soils of the R. Chinit area, Kompong Thom Province, Cambodia. *J. Plant Nutr.* **1976**, *22*, 409–421. [CrossRef]
5. Papineau, D. Chemically oscillating reactions in the formation of botryoidal malachite. *Am. Min.* **2020**, *105*, 447–454. [CrossRef]
6. Papineau, D.; She, Z.; Dodd, M.S. Chemically-oscillating reactions during the diagenetic oxidation of organic matter and in the formation of granules in late Palaeoproterozoic chert from Lake Superior. *Chem. Geol.* **2017**, *470*, 33–54. [CrossRef]
7. Papineau, D.; Yin, J.; Devine, K.G.; Liu, D.; She, Z. Chemically Oscillating Reactions during the Diagenetic Formation of Ediacaran Siliceous and Carbonate Botryoids. *Minerals* **2021**, *11*, 1060. [CrossRef]
8. Papineau, D. Chemically oscillating reactions as a new model for the formation of mineral patterns in Agate geodes and concretions. *Minerals* **2024**, *14*, 203. [CrossRef]
9. Papineau, D.; Devine, K.; Nogueira, B.A. Self-similar patterns from abiotic decarboxylation metabolism through chemically oscillating reactions: A prebiotic model for the origin of life. *Life* **2023**, *13*, 551. [CrossRef]

10. Dodd, M.S.; Papineau, D.; She, Z.; Fogel, M.L.; Nederbragt, S.; Pirajno, F. Organic remains in late Palaeoproterozoic granular iron formations and implications for the origin of granules. *Precambrian Res.* **2018**, *310*, 133–152. [CrossRef]
11. Varkouhi, S.; Papineau, D.; and Guo, Z. Botryoidal quartz as an abiotic signature in Palaeoarchean cherts of the Pilbara Supergroup, Western Australia. *Precambrian Res.* **2022**, *383*, 106876. [CrossRef]
12. Varkouhi, S.; Papineau, D. Silica botryoids from chemically oscillating reactions and as Precambrian environmental proxies. *Geology* **2023**, *51*, 683–687. [CrossRef]
13. Mason, R.; Li, Y.; Cao, K.; Long, Y.; She, Z.B. Ediacaran macrofossils in Shunyang Valley, Sixi, Three Gorges district, Hubei Province, China. *J. Earth Sci.* **2017**, *28*, 614–621. [CrossRef]
14. Ding, W.; Dong, L.; Sun, Y.; Ma, H.; Xu, Y.; Yang, R.; Peng, Y.; Zhou, C.; Shen, B. Early animal evolution and highly oxygenated seafloor niches hosted by microbial mats. *Sci. Rep.* **2019**, *9*, 13628. [CrossRef]
15. Xiao, S.; Chen, Z.; Pang, K.; Zhou, C.; Yuan, X. The Shibantan Lagerstätte: Insights into the Proterozoic–Phanerozoic transition. *J. Geol. Soc.* **2020**, *178*, 135. [CrossRef]
16. Davies, P.J.; Bubela, B.; Ferguson, J. The formation of ooids. *Sedimentology* **1978**, *25*, 703–730. [CrossRef]
17. Flannery, D.T.; Allwood, A.C.; Hodyss, R.; Summons, R.E.; Tuite, M.; Walter, M.R.; Williford, K.H. Microbially influenced formation of Neoarchean ooids. *Geobiology* **2019**, *17*, 151–160. [CrossRef]
18. Lebron, I.; Suarez, D.L. Calcite nucleation and precipitation kinetics as affected by dissolved organic matter at 25 °C and pH > 7.5. *Geochim. Cosmochim. Ac.* **1996**, *60*, 2765–2776. [CrossRef]
19. Fouke, B.W. Hot-spring Systems Geobiology: Abiotic and biotic influences on travertine formation at Mammoth Hot Springs, Yellowstone National Park, USA. *Sedimentology* **2011**, *58*, 170–219. [CrossRef]
20. Liesegang, R.E. Die Entstehung der Achate. *Zentralblatt Mineral.* **1910**, *11*, 593–597.
21. Keller, J.B.; Rubinow, S.I. Recurrent precipitation and Liesegang rings. *J. Chem. Phys.* **1981**, *74*, 5000–5007. [CrossRef]
22. Merino, E. Survey of geochemical self-patterning phenomena. In Nicolis, G. and Baras, F. eds. Chemical Instabilities: Applications in Chemistry Engineering Geology and Materials Science. *NATO Adv. Sci. Ser. C* **1984**, *120*, 305–328.
23. Sultan, R.F.; Abdel-Rahman, M. On dynamic self-organization: Examples from magmatic and other geochemical systems. *Lat. Am. J. Solids Struct.* **2013**, *10*, 59–73. [CrossRef]
24. Nabika, H.; Itatani, M.; Lagzi, I. Pattern Formation in Precipitation Reactions: The Liesegang Phenomenon. *Langmuir* **2019**, *36*, 481–497. [CrossRef] [PubMed]
25. Bosak, T.; Bush, J.W.M.; Flynn, M.R.; Liang, B.; Ono, S.; Petroff, A.P.; Sim, M.S. Formation and stability of oxygen-rich bubbles that shape photosynthetic mats. *Geobiology* **2010**, *8*, 45–55. [CrossRef] [PubMed]
26. Dahanayake, K.; Gerdes, G.; Krumbein, W.E. Stromatolites, oncolites and oolites biogenically formed in situ. *Naturwissenschaften* **1985**, *72*, 513–518. [CrossRef]
27. Dahanayake, K.; Krumbein, W.E. Microbial structures in oolitic iron formations. *Miner. Depos.* **1986**, *21*, 85–94. [CrossRef]
28. Glasauer, S.; Mattes, A.; Gehring, A. Constraints on the Preservation of Ferriferous Microfossils. *Geomicrobiol. J.* **2013**, *30*, 479–489. [CrossRef]
29. Salama, W.; El Aref, M.M.; Gaupp, R. Mineral evolution and processes of ferruginous microbialite accretion—An example from the Middle Eocene stromatolitic and ooidal ironstones of the Bahariya Depression, Western Desert, Egypt. *Geobiology* **2012**, *11*, 15–28. [CrossRef]
30. Diaz, M.R.; Eberli, G.P. Decoding the mechanism of formation in marine ooids: A review. *Earth-Sci. Rev.* **2019**, *190*, 536–556. [CrossRef]
31. Papineau, D.; De Gregorio, B.; Fearn, S.; Kilcoyne, D.; McMahon, G.; Purohit, R.; Fogel, M. Nanoscale petrographic and geochemical insights on the origin of the Palaeoproterozoic stromatolitic phosphorites from Aravalli Supergroup, India. *Geobiology* **2016**, *14*, 3–32. [CrossRef] [PubMed]
32. Zaikin, A.N.; Zhabotinsky, A.M. Concentration Wave Propagation in Two-dimensional liquid-phase self-oscillating system. *Nature* **1970**, *225*, 535–537. [CrossRef] [PubMed]
33. Briggs, T.S.; Rauscher, W.C. An oscillating iodine clock. *J. Chem. Educ.* **1973**, *50*, 496. [CrossRef]
34. Körös, E.; Orbán, M. Uncatalysed oscillatory chemical reactions. *Nature* **1978**, *273*, 371–372. [CrossRef]
35. Epstein, I.R.; Kustin, K.; De Kepper, P.; Orbán, M. Oscillating chemical reactions. *Sci. Am.* **1983**, *248*, 112–123. [CrossRef]
36. Agladze, K.I.; Krinsky, V.I.; Pertsov, A.M. Chaos in the non-stirred Belousov–Zhabotinsky reaction is induced by interaction of waves and stationary dissipative structures. *Nature* **1984**, *308*, 834–835. [CrossRef]
37. Field, R.J.; Schneider, F.W. Oscillating chemical reactions and nonlinear dynamics. *J. Chem. Educ.* **1989**, *66*, 195. [CrossRef]
38. Zhabotinsky, A.M. A history of chemical oscillations and waves. *Chaos* **1991**, *1*, 379–386. [CrossRef]
39. Belmonte, A.L.; Ouyang, Q.; Flesselles, J.M. Experimental survey of spiral dynamics in the Belousov-Zhabotinsky reaction. *J. Phys.* **1997**, *7*, 1425–1468. [CrossRef]
40. Orbán, M.; Kurin-Csörgei, K.; Zhabotinsky, A.M.; Epstein, I.R. A new chemical system for studying pattern formation: Bromate–hypophosphite–acetone–dual catalyst. *Faraday Discuss.* **2001**, *120*, 11–19. [CrossRef]
41. Chen, I.C.; Kuksenok, O.; Yashin, V.V.; Moslin, R.M.; Balazs, A.C.; Van Vliet, K.J. Shape-and size-dependent patterns in self-oscillating polymer gels. *Soft Matter* **2011**, *7*, 3141–3146. [CrossRef]
42. Brasier, M.D.; Lindsay, J.F. A billion years of environmental stability and the emergence of eukaryotes: New data from northern Australia. *Geology* **1998**, *26*, 555–558. [CrossRef] [PubMed]

43. Holland, H.D. The oxygenation of the atmosphere and oceans. *Phil. Trans. R. Soc. B* **2006**, *361*, 903–915. [CrossRef] [PubMed]
44. Mitchell, R.N.; Evans, D.A.D. The balanced billion. *GSA Today* **2024**, *34*, 10–11. [CrossRef]
45. Mukherjee, I.; Large, R.R.; Corkrey, R.; Danyushevsky, L.V. The Boring Billion, a slingshot for Complex Life on Earth. *Sci. Rep.* **2018**, *8*, 4432. [CrossRef]
46. Merdith, A.S.; Collins, A.S.; Williams, S.E.; Pisarevsky, S.; Foden, J.D.; Archibald, D.B.; Blades, M.L.; Alessio, B.L.; Armistead, S.; Plavsa, D.; et al. A full-plate global reconstruction of the Neoproterozoic. *Gondwana Res.* **2017**, *50*, 84–134. [CrossRef]
47. Fike, D.A.; Grotzinger, J.P.; Pratt, L.M.; Summons, R.E. Oxidation of the Ediacaran Ocean. *Nature* **2006**, *444*, 744–747. [CrossRef]
48. Jiang, G.; Kennedy, M.; Christie-Blick, N. Stable isotopic evidence for methane seeps in neoproterozoic postglacial cap carbonates. *Nature* **2003**, *426*, 822–826. [CrossRef]
49. Bristow, T.F.; Bonifacie, M.; Derkowski, A.; Eiler, J.M.; Grotzinger, J.P. A hydrothermal origin for isotopically anomalous cap dolostone cements from south China. *Nature* **2011**, *474*, 68–71. [CrossRef]
50. Ader, M.; Macouin, M.; Trindade, R.I.F.; Hadrien, M.; Yang, Z.Y.; Sun, Z.M.; Besse, J. A multilayered water column in the Ediacaran Yangtze platform? Insights from carbonate and organic matter paired $\delta^{13}$C. *Earth Planet. Sci. Lett.* **2009**, *288*, 213–227. [CrossRef]
51. Shields, G.A.; Mills, B.J.W.; Zhu, M.; Raub, T.D.; Daines, S.J.; Lenton, T.M. Unique Neoproterozoic carbon isotope excursions sustained by coupled evaporite dissolution and pyrite burial. *Nat. Geosci.* **2019**, *12*, 823–827. [CrossRef]
52. Li, D.; Luo, G.; Yang, H.; She, Z.; Papineau, D.; Li, C. Characteristics of the carbon cycle in late Mesoproterozoic: Evidence from carbon isotope composition of paired carbonate and organic matter of the Shennongjia Group in South China. *Precambrian Res.* **2022**, *377*, 106726. [CrossRef]
53. Wang, J.; He, Z.; Zhu, D.; Liu, Q.; Ding, Q.; Li, S.; Zhang, D. Petrological and geochemical characteristics of the botryoidal dolomite of Dengying Formation in the Yangtze Craton, South China: Constraints on terminal Ediacaran "dolomite seas". *Sediment. Geol.* **2020**, *406*, 105722. [CrossRef]
54. Zhai, X.; Luo, P.; Gu, Z.; Jiang, H.; Zhang, B.; Wang, Z.; Wang, T.; Wu, S. Microbial mineralization of botryoidal laminations in the Upper Ediacaran dolostones, Western Yangtze Platform, SW China. *J. Asian Earth Sci.* **2020**, *195*, 104334. [CrossRef]
55. Wood, R.A.; Grotzinger, J.P.; Dickson, J.A.D. Proterozoic modular biomineralized metazoan from the Nama Group, Namibia. *Science* **2002**, *296*, 2383–2386. [CrossRef]
56. Meinhold, G.; Roberts, N.M.W.; Arslan, A.; Jensen, S.; Ebbestad, J.O.R.; Högström, A.E.S.; Høyberget, M.; Agić, H.; Palacios, T.; Taylor, W.L. U–Pb dating of calcite in ancient carbonates for age estimates of syn- to post-depositional processes: A case study from the upper Ediacaran strata of Finnmark, Arctic Norway. *Geol. Mag.* **2020**, *157*, 1367–1372. [CrossRef]
57. Gehling, J.G. Environmental interpretation and a sequence stratigraphic framework for the terminal Proterozoic Ediacara Member within the Rawnsley Quartzite, South Australia. *Precambrian Res.* **2000**, *100*, 65–95. [CrossRef]
58. Allison, C.W.; Awramik, S.M. Organic-walled microfossils from earliest Cambrian or latest Proterozoic Tindir Group rocks, northwest Canada. *Precambrian Res.* **1989**, *43*, 253–294. [CrossRef]
59. Leblanc, M.; Billaud, P. Cobalt arsenide orebodies related to an upper Proterozoic ophiolite; Bou Azzer (Morocco). *Econ. Geol.* **1982**, *77*, 162–175. [CrossRef]
60. Sarkar, S.; Choudhuri, A.; Banerjee, S.; Van Loon, A.J.; Bose, P.K. Seismic and non-seismic soft-sediment deformation structures in the Proterozoic Bhander Limestone, central India. *Geologos* **2014**, *20*, 89–103. [CrossRef]
61. Pandey, S.K.; Kumar, S. Organic walled microbiota from the silicified algal clasts, Bhander limestone, Satna area, Madhya Pradesh. *J. Geol. Soc. India* **2013**, *82*, 499–508. [CrossRef]
62. Xiaofeng, W.; Erdtmann, B.D.; Xiaohong, C.; Xiaodong, M. Integrated sequence-, bio- and chemostratigraphy of the terminal Proterozoic to Lowermost Cambrian "black rock series" from central South China. *Episodes* **1998**, *21*, 178–189. [CrossRef]
63. She, Z.; Strother, P.; McMahon, G.; Nittler, L.R.; Wang, J.; Zhang, J.; Sang, L.; Ma, C.; Papineau, D. Terminal Proterozoic cyanobacterial blooms and phosphogenesis documented by the Doushantuo granular phosphorites I: In situ micro-analysis of textures and composition. *Precambrian Res.* **2013**, *235*, 20–35. [CrossRef]
64. Walter, M.R.; Bauld, J. The association of sulphate evaporites, stromatolitic carbonates and glacial sediments: Examples from the Proterozoic of Australia and the Cainozoic of Antarctica. *Precambrian Res.* **1983**, *21*, 129–148. [CrossRef]
65. Normington, V.J.; Beyer, E.E.; Whelan, J.A.; Edgoose, C.J.; Woodhead, J.D. Summary of results—NTGS LA-ICP-MS Hf program: Amadeus Basin, July 2013–June 2015. *North. Territ. Geol. Surv. Rec.* **2019**, *5*, 34.
66. Donnelly, T.H.; Jackson, M.J. Sedimentology and geochemistry of a mid-Proterozoic lacustrine unit from northern Australia. *Sediment. Geol.* **1988**, *58*, 145–169. [CrossRef]
67. Knoll, A.H.; Hayes, J.M.; Kaufman, A.J.; Swett, K.; Lambert, I.B. Secular variation in carbon isotope ratios from Upper Proterozoic successions of Svalbard and East Greenland. *Nature* **1986**, *321*, 832–838. [CrossRef]
68. Knoll, A.H.; Swett, K.; Burkhardt, E. Paleoenvironmental distribution of microfossils and stromatolites in the Upper Proterozoic Backlundtoppen Formation, Spitsbergen. *J. Paleontol.* **1989**, *63*, 129–145. [CrossRef]
69. Zempolich, W.G.; Wilkinson, B.H.; Lohmann, K.C. Diagenesis of late Proterozoic carbonates—The Beck Spring Dolomite of eastern California. *J. Sed. Pet.* **1988**, *58*, 656–672.
70. Smith, E.F.; MacDonald, F.A.; Crowley, J.L.; Hodgin, E.B.; Schrag, D.P. Tectonostratigraphic evolution of the c. 780–730 Ma Beck Spring Dolomite: Basin Formation in the core of Rodinia. *Geol. Soc. Spec. Publ.* **2016**, *424*, 213–239. [CrossRef]

71. Southgate, P.N. Depositional environment and mechanism of preservation of microfossils, upper Proterozoic Bitter Springs Formation, Australia. *Geology* **1986**, *14*, 683–686. [CrossRef]
72. Schopf, J.W.; Kudryavtsev, A.B.; Sugitani, K.; Walter, M.R. Precambrian microbe-like pseudofossils: A promising solution to the problem. *Precambrian Res.* **2010**, *179*, 191–205. [CrossRef]
73. Bull, S.; Selley, D.; Broughton, D.; Hitzman, M.; Cailteux, J.; Large, R.; McGoldrick, P. Sequence and carbon isotopic stratigraphy of the Neoproterozoic Roan Group strata of the Zambian copperbelt. *Precambrian Res.* **2011**, *190*, 70–89. [CrossRef]
74. Rowlands, N.J.; Blight, P.G.; Jarvis, D.M.; Von Der Borch, C.C. Sabkha and playa environments in late Proterozoic grabens, Willouran Ranges, South Australia. *J. Geol. Soc. Aust.* **1980**, *27*, 55–68. [CrossRef]
75. Rowan, M.G.; Hearon IV, T.E.; Kernen, R.A.; Giles, K.A.; Gannaway-Dalton, C.E.; Williams, N.J.; Fiduk, J.C.; Lawton, T.F.; Hannah, P.T.; Fischer, M.P. A review of allochthonous salt tectonics in the Flinders and Willouran ranges, South Australia. *Aust. J. Earth Sci.* **2019**, *67*, 787–813. [CrossRef]
76. Turner, E.C.; Narbonne, G.M.; James, N.P. Neoproterozoic reef microstructures from the Little Dal Group, northwestern Canada. *Geology* **1993**, *21*, 259–262. [CrossRef]
77. Hofmann, H.J.; Altken, J.D. Precambrian biota from the Little Dal Group, Mackenzie Mountains, northwestern Canada. *Can. J. Earth Sci.* **1979**, *16*, 150–166. [CrossRef]
78. Kinnaird, T.C.; Prave, A.R.; Kirkland, C.; Horstwood, M.; Parrish, R.; Batchelor, R.A. The late Mesoproterozoic–early Neoproterozoic tectonostratigraphic evolution of NW Scotland: The Torridonian revisited. *J. Geol. Soc.* **2007**, *164*, 541–551. [CrossRef]
79. Kaufman, A.J.; Hayes, J.M.; Knoll, A.H.; Germs, G.J. Isotopic compositions of carbonates and organic carbon from upper Proterozoic successions in Namibia: Stratigraphic variation and the effects of diagenesis and metamorphism. *Precambrian Res.* **1991**, *49*, 301–327. [CrossRef]
80. Nascimento, D.B.; Schmitt, R.S.; Ribeiro, A.; Trouw, R.A.; Passchier, C.W.; Basei, M.A. Depositional ages and provenance of the Neoproterozoic Damara Supergroup (northwest Namibia): Implications for the Angola-Congo and Kalahari cratons connection. *Gondwana Res.* **2017**, *52*, 153–171. [CrossRef]
81. Skotnicki, S.J.; Knauth, L.P. The Middle Proterozoic Mescal Paleokarst, Central Arizona, U.S.A.: Karst Development, Silicification, and Cave Deposits. *J. Sediment. Res.* **2007**, *77*, 1046–1062. [CrossRef]
82. White, D. Algal Deposits of Unkar Proterozoic Age in the Grand Canyon, Arizona. *Proc. Natl. Acad.Sci. USA* **1928**, *14*, 597–600. [CrossRef] [PubMed]
83. Timmons, J.M.; Karlstrom, K.E.; Heizler, M.T.; Bowring, S.A.; Gehrels, G.E.; Crossey, L.J. Tectonic inferences from the ca. 1255–1100 Ma Unkar Group and Nankoweap Formation, Grand Canyon: Intracratonic deformation and basin formation during protracted Grenville orogenesis. *Geol. Soc. Am. Bull.* **2005**, *117*, 1573–1595. [CrossRef]
84. Ostwald, J.; Bolton, B.R. Diagenetic braunite in sedimentary rocks of the Proterozoic Manganese Group, Western Australia. *Ore Geol. Rev.* **1990**, *5*, 315–323. [CrossRef]
85. Goode, A.D.T.; Hall, W.D.M. The middle Proterozoic Eastern Bangemall Basin, Western Australia. *Precambrian Res.* **1981**, *16*, 11–29. [CrossRef]
86. Blake, T.S.; Rothery, E.; Muhling, J.R.; Drake-Brockman, J.A.P.; Sprigg, L.C.; Ho, S.E.; Rasmussen, B.; Fletcher, I.R. Two episodes of regional-scale Precambrian hydrothermal alteration in the eastern Pilbara, Western Australia. *Precambrian Res.* **2011**, *188*, 73–103. [CrossRef]
87. Collinson, J.D. Sedimentology of unconformities within a fluvio-lacustrine sequence; Middle Proterozoic of Eastern North Greenland. *Sediment. Geol.* **1983**, *34*, 145–166. [CrossRef]
88. Strauss, H.; Schieber, J. A sulfur isotope study of pyrite genesis: The mid-proterozoic Newland Formation, Belt Supergroup, Montana. *Geochim. et Cosmochim. Acta* **1990**, *54*, 197–204. [CrossRef]
89. Wang, X.; Zhang, S.; Wang, H.; Canfield, D.E.; Su, J.; Hammarlund, E.U.; Bian, L. Remarkable preservation of microfossils and biofilms in Mesoproterozoic silicified bitumen concretions from northern China. *Geofluids* **2017**, *2017*, 1–12. [CrossRef]
90. Liu, A.Q.; Tang, D.J.; Shi, X.Y.; Zhou, L.M.; Zhou, X.Q.; Shang, M.H.; Li, Y.; Song, H.Y. Growth mechanisms and environmental implications of carbonate concretions from the~ 1.4 Ga Xiamaling Formation, North China. *J. Palaeogeogr.* **2019**, *8*, 20. [CrossRef]
91. Liu, A.; Tang, D.; Shi, X.; Zhou, X.; Zhou, L.; Shang, M.; Li, Y.; Fang, H. Mesoproterozoic oxygenated deep seawater recorded by early diagenetic carbonate concretions from the Member IV of the Xiamaling Formation, North China. *Precambrian Res.* **2020**, *341*, 105667. [CrossRef]
92. Pratt, B.R. Molar-tooth structure in Proterozoic carbonate rocks: Origin from synsedimentary earthquakes, and implications for the nature and evolution of basins and marine sediment. *Geol. Soc. Am. Bull.* **1998**, *110*, 1028–1045. [CrossRef]
93. Walker, R.N.; Muir, M.D.; Diver, W.L.; Williams, N.; Wilkins, N. Evidence of major sulphate evaporite deposits in the Proterozoic McArthur Group, Northern Territory, Australia. *Nature* **1977**, *265*, 526–529. [CrossRef]
94. Luo, J.; Long, X.; Bowyer, F.T.; Mills, B.J.W.; Li, J.; Xiong, Y.; Zhu, X.; Zhang, K.; Poulton, S.W. Pulsed oxygenation events drove progressive oxygenation of the early Mesoproterozoic ocean. *Earth Planet. Sci. Lett.* **2021**, *559*, 116754. [CrossRef]
95. McClay, K.R.; Carlile, D.G. Mid-Proterozoic sulphate evaporites at Mount Isa mine, Queensland, Australia. *Nature* **1978**, *274*, 240–241. [CrossRef]
96. Tang, D.; Shi, X.; Wang, X.; Jiang, G. Extremely low oxygen concentration in mid-Proterozoic shallow seawaters. *Precambrian Res.* **2016**, *276*, 145–157. [CrossRef]

97. Cabral, A.R.; Lehmann, B.; Tupinambá, M.; Schlosser, S.; Kwitko-Ribeiro, R.; de Abreu, F.R. The platiniferous Au-Pd belt of Minas Gerais, Brazil, and genesis of its botryoidal Pt-Pd aggregates. *Econ. Geol.* **2009**, *104*, 1265–1276. [CrossRef]
98. Symons, D.T.A. Paleomagnetism of the HYC Zn-Pb SEDEX deposit, Australia: Evidence of an epigenetic origin. *Econ. Geol.* **2007**, *102*, 1295–1310. [CrossRef]
99. Walter, M.R.; Goode, A.D.T.; Hall, W.D.M. Microfossils from a newly discovered Precambrian stromatolitic iron formation in Western Australia. *Nature* **1976**, *261*, 221–223. [CrossRef]
100. Kyser, T.K.; Hiatt, E.E.; Renac, C.; Durocher, K.; Holk, G.J.; Deckart, K. Diagenetic fluids in Paleo-and Meso-Proterozoic sedimentary basins and their implications for long protracted fluid histories. *Short Course Ser.—Miner. Assoc. Can.* **2000**, *28*, 225–262.
101. Cañadas, F.; Papineau, D.; She, Z. Biotic and abiotic processes in Ediacaran spheroid formation. *Front. Earth Sci* **2024**, *12*, 1405220. [CrossRef]
102. Och, L.M.; Shields-Zhou, G.A. The Neoproterozoic oxygenation event: Environmental perturbations and biogeochemical cycling. *Earth-Sci. Rev.* **2012**, *110*, 26–57. [CrossRef]
103. Vidal, C.; Pagola, A. Observed properties of trigger waves close to the center of the target patterns in an oscillating Belousov-Zhabotinskii reagent. *J. Phys. Chem.* **1989**, *93*, 2711–2716. [CrossRef]
104. Hastings, H.M.; Field, R.J.; Sobel, S.G. Microscopic fluctuations and pattern formation in a supercritical oscillatory chemical system. *J. Chem. Phys.* **2003**, *119*, 3291–3296. [CrossRef]
105. Bernard, S.; Benzerara, K.; Beyssac, O.; Menguy, N.; Guyot, F.; Brown Jr, G.E.; Goffé, B. Exceptional preservation of fossil plant spores in high-pressure metamorphic rocks. *Earth Planet. Sci. Lett.* **2007**, *262*, 257–272. [CrossRef]
106. Griffin, J.D.; Zeller, M.A.; Nicewicz, D.A. Hydrodecarboxylation of carboxylic and malonic acid derivatives via organic photoredox catalysis: Substrate scope and mechanistic insight. *J. Am. Chem. Soc.* **2015**, *137*, 11340–11348. [CrossRef]
107. Sheik, C.S.; Cleaves, H.J.; Johnson-Finn, K.; Giovannelli, D.; Kieft, T.L.; Papineau, D.; Schrenk, M.O.; Tumiati, S. Abiotic and biotic processes that drive carboxylation and decarboxylation reactions. *Am. Min.* **2020**, *105*, 609–615. [CrossRef]
108. Rueter, P.; Rabus, R.; Wilkest, H.; Aeckersberg, F.; Rainey, F.A.; Jannasch, H.W.; Widdel, F. Anaerobic oxidation of hydrocarbons in crude oil by new types of sulphate-reducing bacteria. *Nature* **1994**, *372*, 455–458. [CrossRef]
109. Muyzer, G.; Stams, A.J. The ecology and biotechnology of sulphate-reducing bacteria. *Nat. Rev. Microbiol.* **2008**, *6*, 441–454. [CrossRef]
110. Simonson, B.M. Origin and evolution of large Precambrian iron formations. In *Extreme Depositional Environments: Mega End Members in Geologic Time*; Chan, M.A., Archer, A.W., Eds.; The Geological Society of America: Boulder, CO, USA, 2003; pp. 231–244.
111. Pufahl, P.K.; Fralick, P.W. Depositional controls on Palaeoproterozoic iron formation accumulation, Gogebic Range, Lake Superior region, USA. *Sedimentology* **2004**, *51*, 791–808. [CrossRef]
112. Akin, S.J.; Pufahl, P.K.; Hiatt, E.E.; Pirajno, F. Oxygenation of shallow marine environments and chemical sedimentation in Palaeoproterozoic peritidal settings: Frere Formation, Western Australia. *Sedimentology* **2013**, *60*, 1559–1582. [CrossRef]
113. Smith, A.J.B.; Beukes, N.J.; Gutzmer, J.; Czaja, A.D.; Johnson, C.M.; Nhleko, N. Oncoidal granular iron formation in the Mesoarchaean Pongola Supergroup, southern Africa: Textural and geochemical evidence for biological activity during iron deposition. *Geobiology* **2017**, *15*, 731–749. [CrossRef] [PubMed]
114. Hardisty, D.S.; Lu, Z.; Bekker, A.; Diamond, C.W.; Gill, B.C.; Jiang, G.; Kah, L.C.; Knoll, A.H.; Loyd, S.J.; Osburn, M.R.; et al. Perspectives on Proterozoic surface ocean redox from iodine contents in ancient and recent carbonate. *Earth Planet. Sci. Lett.* **2017**, *463*, 159–170. [CrossRef]
115. Ross, G.M.; Bloch, J.D.; Krouse, H.R. Neoproterozoic strata of the southern Canadian Cordillera and the isotopic evolution of seawater sulfate. *Precambrian Res.* **1995**, *73*, 71–99. [CrossRef]
116. Hurtgen, M.T.; Arthur, M.A.; Halverson, G.P. Neoproterozoic sulfur isotopes, the evolution of microbial sulfur species, and the burial efficiency of sulfide as sedimentary pyrite. *Geology* **2005**, *33*, 41–44. [CrossRef]
117. Canfield, D.E.; Raiswell, R. The evolution of the sulfur cycle. *Am. J. Sci.* **1999**, *299*, 697–723. [CrossRef]
118. McCollom, T.M.; Ritter, G.; Simoneit, B.R. Lipid synthesis under hydrothermal conditions by Fischer-Tropsch-type reactions. *Orig. Life Evol. Biosph.* **1999**, *29*, 153–166. [CrossRef]


**Disclaimer/Publisher's Note:** The statements, opinions and data contained in all publications are solely those of the individual author(s) and contributor(s) and not of MDPI and/or the editor(s). MDPI and/or the editor(s) disclaim responsibility for any injury to people or property resulting from any ideas, methods, instructions or products referred to in the content.